1

Introduction to Mobile Magnetic Actuation System

1.1 Introduction

In recent years, miniature robots have increasingly captured the focus of researchers and practitioners, primarily owing to their substantial potential in medical and bioengineering fields [1–3]. The definition of a "miniature robot" pertains to a device that is controllable and has dimensions spanning from micrometers to millimeters. Due to their small size, these robots can access intricate and confined areas within the human body in a minimally invasive fashion, including the gastrointestinal (GI) tract, vasculature, brain, and eye. Furthermore, they possess the capability to carry out a variety of tasks, such as targeted drug delivery [4], precision surgical operations [5, 6], and comprehensive medical examinations [7]. Besides, microsized robots hold promise for in vitro applications, like cell manipulation and tissue engineering, because they can manipulate subcellular entities with high precision and repeatability.

Given their small size, the newly developed tiny agents hold great promise for transforming medical diagnosis and treatment via minimally invasive techniques. Nevertheless, incorporating conventional onboard components, including actuators, processors, and power sources, poses significant difficulties in submillimeter robots due to their constrained volume. Consequently, researchers have directed their efforts toward remote actuation methods to achieve wireless control of untethered robots. The proposed approaches encompass optical [8], acoustically controlled [9, 10], chemical reaction, and magnetic field-based methods [11].

Optical tweezers, as highly sensitive and versatile tools, are capable of trapping cells and microparticles. However, their penetration depth within the body is limited, resulting in insufficient force for practical applications. Acoustically controlled methods offer a non-harmful driving force for specially engineered microrobots inside the human body, yet precise control over their direction and trajectory remains elusive, with research in this area still in its infancy. Chemical reaction methods can propel microrobots forward, but managing the chemical changes induced in the body proves to be a formidable challenge. In contrast, the magnetic field method enables wireless actuation of magnetic robots without signal attenuation during penetration through the human body. Magnetically controlled microrobots can be precisely guided to navigate within living organisms, addressing a multitude of medical issues. However, magnetic actuation is not without its drawbacks, including a confined workspace, restricted magnetic flux density for actuation, and the bulkiness and costliness of the designed system. Therefore, the development of magnetic actuation systems (MASs) has been geared toward overcoming these limitations.

The inherently interdisciplinary nature of MASs in clinical settings underscores the need for coordinated efforts among a diverse group of experts, encompassing roboticists, clinical practitioners, regenerative medicine researchers, and biomedical engineers. Clinical specialists blend conventional approaches with engineering insights to devise innovative solutions to prevailing challenges [12].

Simultaneously, regenerative medicine scientists have been refining stem cell modifications to elicit therapeutic outcomes at designated target locations. Within the realm of biomedical engineering, magnetic micro/millirobots (MMRs) have been harnessed as delivery vehicles to achieve pinpoint drug administration through closed-loop control mechanisms [13, 14]. Notably, the development of MASs for clinical use by roboticists and engineers serves as the cornerstone that supports and enables all these collaborative initiatives [15–17]. The fusion of specialized knowledge and concerted efforts across these disciplines drives progress and fosters innovations that hold immense promise for the future landscape of medical robotics.

The traditional paradigm of medical treatment commonly involves introducing high-dosage medications into patients via the bloodstream, relying on passive transport. Nevertheless, this approach has inherent drawbacks. A substantial amount of the medication can be taken up by nontargeted organs or cells, which may lead to side effects and harm to the body. Consequently, there is a pressing need for a more accurate and controlled drug delivery mechanism. MASs offer the capability of precise, wireless control over magnetic robots, facilitating targeted delivery and controlled movement within the body. This unique feature unlocks a wide array of clinical applications. In addition to precision drug delivery, MMRs, when actuated by MASs, can be employed to deliver functional cells, such as stem cells, to specific sites for repairing damaged cartilage. Moreover, MASs are relevant in various scenarios requiring precise delivery, such as removing blood clots from the cardiovascular system and performing vitreoretinal or GI endoscopy. Addressing these diverse applications requires the development of suitable MASs and MMRs that are tailored for clinical use. Significant attention has been devoted to advancing the MAS and MMR designs to satisfy the specific needs of clinical applications, emphasizing their potential to revolutionize the field of medicine.

The development of actuation systems for clinical applications is accompanied by inherent challenges. A critical issue stems from the intrinsic properties of MASs. From an energy perspective, the natural instability of the dipole in all directions poses a significant obstacle to the effective control of permanent MASs. Additionally, the magnetic field strength decreases rapidly as it moves away from the source, following a cubic distance decay pattern. This rapid attenuation renders the field unsuitable for many applications where sustained strength is required. Furthermore, even when the magnetic field is amplified at the center of the workspace, the steep gradients near the electromagnet limit the effective operational area to a region smaller than the full 3D environment. This constraint adds complexity to the design of MASs for real-world practical use.

In response to the challenges inherent in MAS design, researchers have adopted the closed-loop flux path method to boost magnetic field intensity and gradient. When integrated with appropriate mapping strategies, this system can function as a magnetic catheter guidance platform. A thorough examination of magnetic field distribution across the workspace and between electromagnets is critical for calculating the precise current levels needed to accomplish specific tasks [18]. Strict current regulation is necessary to prevent excessive heating, which could compromise wire integrity. Moreover, the effective operational workspace for many practical applications remains constrained. To address these limitations, recent studies have focused on innovations such as optimized wire configurations and advanced coil designs [19]. These advancements aim to elevate manipulation capabilities and extend the boundaries of magnetic actuation in intricate clinical scenarios.

The efficient control of MMRs is paramount to their operational performance, particularly when these robots collaborate to execute intricate tasks. A robot's morphological design profoundly influences its control dynamics and functional capabilities. Presently, significant research efforts have been directed toward understanding core locomotion mechanisms—such as slipping, rolling, walking, and climbing—as these foundational modes can be integrated to achieve diverse operational objectives [20]. A critical consideration in MMR design is material selection, which must prioritize magnetizable properties while ensuring biocompatibility (non-cytotoxicity). Notably, recent advancements have centered on developing MMRs using materials that are both biodegradable and magnetizable, aiming to create robots capable of completing tasks and subsequently degrading safely within the body [21, 22]. The objective is to enable precise navigation and propulsion by integrating multiple locomotion strategies. Beyond robot design, the development of MASs capable of generating sufficiently strong magnetic field gradients or torque within expansive workspaces is equally essential. This aspect has been a focal point in the literature, with studies emphasizing the need for MAS designs that ensure accurate, high-gradient magnetic fields during MMR navigation [23, 24]. Collectively, these advancements form the foundation for medical interventions leveraging magnetic manipulation techniques.

Beyond the technical optimization of MASs and MMRs, the operational success of magnetic manipulation systems hinges critically on real-time feedback derived from advanced imaging modalities. Among these, photoacoustic imaging has emerged as a particularly promising in vivo imaging technique [25], garnering significant interest for its utility in providing precise feedback signals for contemporary research applications. Depending on the application context, alternative imaging approaches such as fluoroscopy or magnetic resonance imaging (MRI) may also be employed. However, these methods are accompanied by notable limitations, including potential health risks associated with prolonged exposure (e.g., ionizing radiation in fluoroscopy) and the inherently time-consuming nature of MRI protocols. Collectively, these factors underscore the need for careful selection and integration of imaging technologies to balance feedback quality with practical constraints in clinical settings.

The control of magnetic robots can be broadly categorized into three paradigms: individual manipulation, coordinated multi-agent systems, and large-scale swarm control [26, 27]. The incorporation of machine learning algorithms and optimization strategies further elevates operational efficiency and precision [28]. These advanced methodologies have yielded encouraging outcomes, particularly in enabling accurate drug delivery within intricate three-dimensional (3D) environments—a critical capability for targeted medical interventions.

1.2 Magnetic Actuation Systems

1.2.1 Magnetic Actuation Principle

Magnetic actuation operates by exerting forces or torques on magnetic entities—either embedded with permanent magnets or composed of magnetizable materials—through externally controlled magnetic fields (see Figure 1.1). Notably, the absence of electrical currents within the operational environment allows the quasistatic magnetic field to be rigorously modeled using Maxwell’s equations, as established in [29]. This framework provides a foundational basis for analyzing and optimizing magnetic manipulation systems.

$$\nabla \cdot \mathbf{B} = 0 \quad \nabla \times \mathbf{B} = 0 \tag{1.1}$$

where $\mathbf{B}$ is the external magnetic field and ∇ is the gradient operator. The equation implies that the gradient matrix of $\mathbf{B}$ is symmetric and trace free. A magnetic torque $\boldsymbol{\tau}$ acts on a magnetic object m when misalignment occurs between the magnetization of the object and the orientation of the magnetic field as follows:

$$\tau = \mathbf{m} \times \mathbf{B} = \begin{bmatrix} 0 & B_z & -B_y \\ -B_x & 0 & B_x \\ B_y & -B_x & 0 \end{bmatrix} \begin{bmatrix} m_x \\ m_y \\ m_z \end{bmatrix} \tag{1.2}$$

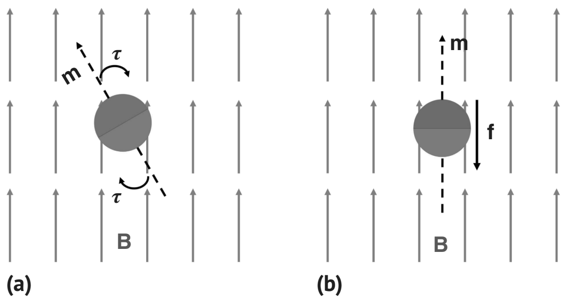

Figure 1.1 Diagram of magnetic interaction. (a) pure torque under a uniform magnetic field; (b) pure force under a nonuniform magnetic field.

Moreover, a magnetic force $\mathbf{f}$ exists, when a magnetic object is in a nonuniform magnetic field as follows:

$$\mathbf{f} = (\mathbf{m} \cdot \nabla)\mathbf{B} = \begin{bmatrix} \dfrac{\partial B_x}{\partial y} & \dfrac{\partial B_y}{\partial y} & \dfrac{\partial B_y}{\partial z} \\ \dfrac{\partial B_x}{\partial z} & \dfrac{\partial B_y}{\partial z} & -\left(\dfrac{\partial B_x}{\partial x} + \dfrac{\partial B_y}{\partial y}\right) \end{bmatrix} \begin{bmatrix} m_x \\ m_y \\ m_z \end{bmatrix} \tag{1.3}$$

Either effect can be deployed individually or in concert to achieve six-degree-of-freedom motion. In the analytical framework of Eqs. (1.2) and (1.3), each robot is treated as a magnetic dipole, an assumption justified when its size is dwarfed by the workspace. With full field programmability, the dipole model caps controllable degrees of freedom (DOFs) at five—three for translational force and two for torque—since rotation about the intrinsic magnetization axis is unavailable. A force couple generated by tailored multimagnet architectures reinstates the absent degree and thereby secures complete six-axis guidance [30]. Altogether, the magnetic field offers eight independent coordinates: three field components together with five gradient components.

To characterize the energy field in an electromagnetic manipulation system, the first analytical step relies on the four Maxwell equations, which collectively establish the theoretical basis for modeling both electric and magnetic field behaviors. These equations form the cornerstone for understanding field interactions and energy distribution in such systems.

$$\nabla \cdot \mathbf{E} = \frac{\rho}{\varepsilon_0} \tag{1.4}$$

$$\nabla \times \mathbf{E} = -\frac{\partial \mathbf{B}}{\partial t} \tag{1.5}$$

$$\nabla \cdot \mathbf{B} = 0 \tag{1.6}$$

$$\nabla \times \mathbf{B} = \mu_0 \mathbf{J} + \mu_0 \varepsilon_0 \frac{\partial D}{\partial t} \tag{1.7}$$

where **E** represents the electric field strength, related to the electric displacement vector **D** via $\mathbf{E} = \frac{1}{\varepsilon_0}\mathbf{D}$, with ε_0 denoting vacuum permittivity; **B** denotes the magnetic flux density, linked to the magnetic field strength **H** (in A/m) through $\mathbf{B} = \mu_0 \mathbf{H}$, where $\mu_0 = 4\pi \times 10^{-7}\text{H/m}$ is the vacuum permeability. The electric charge density is symbolized by ρ, while **j** corresponds to current density (zero in the manipulation region but non-zero within magnets). Alternative formulations of Maxwell's equations are derived from the foundational Eqs. (1.4)–(1.7).

The magnetic dipole model is widely adopted to describe the spatial variation of magnetic flux density around a single pole of a permanent magnet. For such configurations, the scalar magnetic potential is typically expressed using a Taylor series expansion, which provides a systematic framework for approximating the field's behavior. This approach enables analytical modeling of the magnetic potential's dependence on spatial coordinates near the magnet's pole region.

$$\boldsymbol{\Phi}(r) = \frac{1}{4\pi} \sum_{n=0}^{\infty} \frac{1}{||r||^{n+1}} \oint_S \rho^n \mathrm{P}_n(\mathbf{r} \cdot \rho)(\mathbf{n} \cdot \mathbf{M})\, \mathrm{da} \tag{1.8}$$

where ρ denotes the distance from the magnetic volume's center to the integration point, $\mathrm{P}_n()$ represents Legendre polynomials, **M** is the magnetization vector, **n** is the normal unit vector, and **r** is the position vector from the magnetic volume's center to the point of interest (expressed as $\mathbf{r} = {}^{\mathbf{i}}P_{\mathbf{B}} +^{\mathbf{i}} \mathbf{P_m}$, as illustrated in Figure 1.2a). This formulation simplifies to a multipole expansion when the analysis points lie outside the minimum bounding sphere—the smallest sphere entirely containing the magnet during magnetic flux evaluation.

The magnetic flux density can be represented with an expansion form as:

$$\begin{aligned}\mathbf{B}\{\mathbf{r}, \mathbf{m}\} &= \mu \mathbf{H} = -\mu \nabla \Phi \\ &= \left(\frac{\mu}{4\pi||\mathbf{r}||^2} \mathbb{P}_2\{\hat{\mathbf{r}}\} + \frac{\mu}{4\pi||\mathbf{r}||^3} \mathbb{P}_3\{\hat{\mathbf{r}}\} + \frac{\mu}{4\pi||\mathbf{r}||^4} \mathbb{P}_4\{\hat{\mathbf{r}}\} \right. \\ &\quad \left. + \frac{\mu}{4\pi||\mathbf{r}||^5} \mathbb{P}_5\{\hat{\mathbf{r}}\} + \ldots \right) \mathbf{m}\end{aligned} \tag{1.9}$$

where μ denotes the permeability of the surrounding medium, which is $\mu_0 = 4\pi \times 10^{-7}\ \mathrm{T \cdot m \cdot A^{-1}}$ in free space. This value can vary depending on the medium in which the MMR is placed. The dipole moment **m** is defined as the integral of the magnetization **M** over the volume **V**.

Based on the properties outlined in Eq. (1.6), the even-order terms ($\propto \frac{1}{r^2}$, $\propto \frac{1}{r^4}$, etc.) are nullified in the expanded version of Eq. (1.9). Consequently, the initial

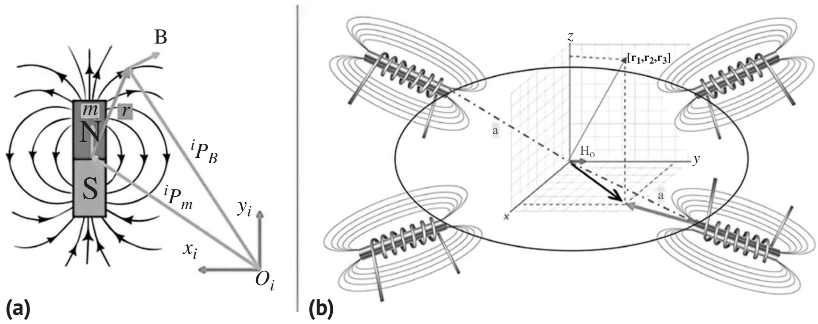

Figure 1.2 Magnetic field illustration. (a) The representation of magnetic flux density around a permanent magnet (represented as a magnetic dipole), where the original coordinate is $x_iO_iy_i$, $\mathbf{m}$ represents the magnetic moment, $\mathbf{B}$ is the magnetic flux density at the position away from the center of the magnetic dipole with a distance $\mathbf{r}$. (b) The multiple electromagnets' field distribution, where the $[\mathbf{r_1}, \mathbf{r_2}, \mathbf{r_3}]$ represents the position under global coordinate, $\mathbf{H_0}$ is the unit magnetic field strength, and $\mathbf{a}$ is the radius of the workspace.

nonzero term in the polynomial expansion is characterized by a decay rate of $||r||^{-3}$ (the dipole term with $n = 2$), followed by subsequent terms that diminish at a rate of $||r||^{-5}$, and so forth.

The magnetic dipole model is frequently employed to estimate magnetic flux density values, particularly when the magnet's geometry and internal magnetization distribution are unknown. This simplified approximation serves as the most commonly referenced approach under such conditions, enabling practical estimation of field strength based on measurable external parameters.

$$\mathbf{B}_{\text{dipole}}(\mathbf{r}) = \frac{\mu_0}{4\pi}\frac{1}{||\mathbf{r}||^3}\left(3\hat{\mathbf{r}}\hat{\mathbf{r}}^T - \mathbb{I}\right)\mathbf{m}; \tag{1.10}$$

where $\hat{\mathbf{r}}$ represents the unit vector of $\mathbf{r}$ and $\mathbb{I} \subseteq \mathbb{R}^{3\times3}$ denotes the identity matrix. As per Eq. (1.10), the dipole field's magnitude diminishes cubically with distance. In terms of geometry optimization for permanent magnets in static MAS, research indicates that cylinders with rectangular cross-sections (with a diameter-to-length ratio of $\sqrt{\frac{4}{3}}$) and cubes are the most effective shapes.

From an energy standpoint, the total energy U_b of a magnetic dipole with a moment $\mathbf{m}$ can be represented as follows.

$$U_b = -\mathbf{m}\cdot\mathbf{B} = -\begin{bmatrix} m_x & m_y & m_z \end{bmatrix}\cdot\begin{bmatrix} B_x \\ B_y \\ B_z \end{bmatrix} \tag{1.11}$$

Earnshaw’s theorem elucidates the inherent instability of a magnetic dipole within an external magnetic field **B**. To achieve stable levitation of the magnetic dipole, it is essential that Eq. (1.8) possess a minimum point. This necessitates the Laplace equation of the total energy U_b to satisfy the condition $\nabla^2 U_b > 0$, ensuring the system’s stability through a positive definiteness in the energy landscape.

Because both the divergence and curl of **B** are zero, the Laplace equation of **B** is zero, that is

$$\begin{aligned}\nabla^2 U_b &= -\frac{\partial^2 \mathbf{m}\cdot\mathbf{B}}{\partial x^2} - \frac{\partial^2 \mathbf{m}\cdot\mathbf{B}}{\partial y^2} - \frac{\partial^2 \mathbf{m}\cdot\mathbf{B}}{\partial z^2} \\ &= -m_x \nabla^2 B_x - m_y \nabla^2 B_y - m_z \nabla^2 B_z = 0\end{aligned} \tag{1.12}$$

Therefore, the dipole cannot reach the minimum or maximum energy points. The dipole cannot be stable in all directions at any point in free space under magnetic field **B**.

To address instability in electromagnetic systems, researchers have explored diverse strategies. One approach involves modifying system accessories to compensate for unstable directions during analysis, while another utilizes magnetic traps to confine objects at specific 2D surface locations [31]. However, these solutions lose efficacy in 3D environments when holding plates or accessories are removed, leading to renewed instability. A related technique in magnetic catheter-based guidance balances mechanical reaction forces with magnetic gradient-generated forces to stabilize objects, though such methods are impractical in complex in vivo clinical environments—a recognized challenge in existing studies [32]. Alternative approaches circumvent Earnshaw’s theorem through dynamic magnetic field control [33]. By applying time-varying currents to electromagnets, researchers create transient trapping points, enabling adaptive applications like targeted radiation therapy and selective embolization in cancer treatment. Most clinical systems rely on open-loop preprogrammed controls, which lack adaptability to dynamic fields. A commonly adopted solution involves integrating perception feedback to enhance magnetic robot control accuracy, stabilizing 3D motion under MAS. The following section elaborates on open-loop and closed-loop control methodologies.

1.2.2 Electromagnetic Field and Force/Torque Analysis

The underlying basis for electromagnetic field generation is outlined in Eq. (1.7), illustrating how a magnetic field forms in response to an applied electric field. Notably, the second term on the right-hand side accounts for the hysteresis effect, which is linked to electric displacement.

The force applied to a magnetic object with magnetic dipole moment $\mathbf{m}$ in field $\mathbf{B}$ can be represented by the following equation.

$$\mathbf{F} = (\mathbf{m} \cdot \nabla)\mathbf{B} \tag{1.13}$$

At room temperature, $\mathbf{m}$ is linearly related to $\mathbf{B}$ for a superparamagnetic under-saturated magnetic robot. The moment can be represented by Eq. (1.14):

$$\mathbf{m} = V_m \mathbf{M} = V_m \frac{\chi_m}{(1 + \chi_m)\mu_0} \mathbf{B} \tag{1.14}$$

where χ_m is the magnetic susceptibility.

According to Eqs. (1.6) and (1.7), the conditions $tr(\nabla \mathbf{B}) = 0$ and the symmetry of $\nabla \mathbf{B}$ are satisfied within an electromagnetic actuation system's workspace for a magnetic object. Consequently, the magnetic force can be expressed accordingly.

$$\mathbf{F} = \begin{bmatrix} \frac{\partial B_x}{\partial x} & \frac{\partial B_x}{\partial y} & \frac{\partial B_x}{\partial z} \\ \frac{\partial B_x}{\partial y} & \frac{\partial B_y}{\partial y} & \frac{\partial B_y}{\partial z} \\ \frac{\partial B_x}{\partial z} & \frac{\partial B_y}{\partial z} & -\left(\frac{\partial B_x}{\partial x} + \frac{\partial B_y}{\partial y}\right) \end{bmatrix} \mathbf{m}$$

$$= \begin{bmatrix} m_x & m_y & m_z & 0 & 0 \\ 0 & m_x & 0 & m_y & m_z \\ -m_z & 0 & m_x & -m_z & m_y \end{bmatrix} \begin{bmatrix} \frac{\partial B_x}{\partial x} \\ \frac{\partial B_x}{\partial y} \\ \frac{\partial B_x}{\partial z} \\ \frac{\partial B_y}{\partial y} \\ \frac{\partial B_y}{\partial z} \end{bmatrix} = \mathcal{F}(\mathbf{m})\mathcal{G}(\nabla \mathbf{B}^{\mathrm{T}}) \tag{1.15}$$

In a simplified scenario where the magnetic field coordinates coincide with the global coordinates, resulting in $\frac{\partial B_x}{\partial y} = \frac{\partial B_x}{\partial z} = \frac{\partial B_y}{\partial z} = 0$, the magnetic force can be simplified further.

$$\mathbf{F} = \begin{bmatrix} m_x & m_y & m_z & 0 & 0 \\ 0 & m_x & 0 & m_y & m_z \\ -m_z & 0 & m_x & -m_z & m_y \end{bmatrix} \begin{bmatrix} \frac{\partial B_x}{\partial x} \\ 0 \\ 0 \\ \frac{\partial B_y}{\partial y} \\ 0 \end{bmatrix} = \begin{bmatrix} m_x \frac{\partial B_x}{\partial x} \\ m_y \frac{\partial B_y}{\partial y} \\ -m_z \left(\frac{\partial B_x}{\partial x} + \frac{\partial B_y}{\partial y} \right) \end{bmatrix} \tag{1.16}$$

Magnetic torque arises from the rotation of the magnetic dipole **m** around an axis, with its direction being perpendicular to both **m** and **B**. For a magnetic dipole **m** positioned at an angle θ_x from the direction of **B** relative to the x-axis, the magnetic torque τ_x is given by the following expression.

$$\tau_x = \frac{\partial(\mathbf{B} \cdot \mathbf{m})}{\partial \theta_x} = \frac{\partial(||B||||m|| \cos(\theta_x))}{\partial \theta_x} = -||B||||m|| \sin(\theta_x) \tag{1.17}$$

The total torque in three dimensions can be represented as:

$$\tau = \mathbf{m} \times \mathbf{B} = \mathrm{Sk}(\mathbf{m})\mathbf{B} = \begin{bmatrix} 0 & -m_z & m_y \\ m_z & 0 & -m_x \\ -m_y & m_x & 0 \end{bmatrix} \begin{bmatrix} B_x \\ B_y \\ B_z \end{bmatrix} \tag{1.18}$$

where Sk(**m**) denotes the skew-symmetric form of the vector **m**×. Unlike the magnetic force, which possesses 3-DOFs, the magnetic torque has only two controllable DOFs. This limitation exists because it is not possible to produce torque about an axis that is aligned with the direction of **m**.

In a MAS system that includes several electromagnets, as depicted in Figure 1.2b, there is a linear relationship between the current applied to the coils and the electromagnetic flux density. The magnetic field at a particular point **p** in the workspace is the aggregate of the magnetic flux densities produced by each individual electromagnet. The principle of superposition is applicable only if the magnetization does not reach saturation. The current is represented by $I = [I_1, I_2, \dots, I_i, \dots, I_n]^T$ (in amperes), and the overall magnetic flux density $\mathbf{B}$ (in Tesla) is given by the following expression.

$$\boldsymbol{B}(\boldsymbol{p}) = \sum_{i=1}^{n} \boldsymbol{B}_i(\boldsymbol{p}) = \sum_{i=1}^{n} \tilde{\boldsymbol{B}}_i(\boldsymbol{p}) I_i \tag{1.19}$$

where $\tilde{\boldsymbol{B}}_i$ is a unit-current vector expressed in Tesla per Ampere.

The partial derivative of $\boldsymbol{B}$ with respect to the x-coordinate at point $\boldsymbol{p}$ in the effective workspace can be represented as follows:

$$\begin{aligned} \frac{\partial \boldsymbol{B}(\boldsymbol{p})}{\partial x} &= \left[\frac{\partial \tilde{\boldsymbol{B}}_1(\boldsymbol{p})}{\partial x}, \quad \cdots, \quad \frac{\partial \tilde{\boldsymbol{B}}_n(\boldsymbol{p})}{\partial x}\right] \left[I_1, \cdots, I_n\right]^T \\ &= \sum_{i=1}^{n} \frac{\partial \tilde{\boldsymbol{B}}_i(\boldsymbol{p})}{\partial x} I_i \end{aligned} \tag{1.20}$$

The initial term in $\mathcal{G}(\nabla \mathbf{B}^{\mathrm{T}})$ of Eq. (1.15), specifically $\frac{\partial B_x}{\partial x}$, can be expressed as $\sum_{i=1}^{n} \frac{\partial(\tilde{B}_{x_i}(\boldsymbol{p}))}{\partial x} I_i$. Correspondingly, the first term in $\mathbf{B}$ of Eq. (1.18), B_x, is represented as $\sum_{i=1}^{n} (\tilde{B}_{x_i}(\boldsymbol{p})) I_i$, where $(\tilde{B}_x)_i(\boldsymbol{p})$ denotes the magnetic flux density in the x direction generated by the ith electromagnet at position $\boldsymbol{p}$.

By incorporating Eqs. (1.15)–(1.20), a compact representation that accounts for a controllable magnetic field and its gradient can be derived, which is expressed as follows:

$$\begin{aligned} \begin{bmatrix} \tau \\ \boldsymbol{F} \end{bmatrix} &= \begin{bmatrix} \mathrm{Sk}(\boldsymbol{m}) & \boldsymbol{O} \\ \boldsymbol{O} & \mathcal{F}(\boldsymbol{m}) \end{bmatrix} \begin{bmatrix} \boldsymbol{B} \\ \mathcal{G}(\nabla \boldsymbol{B}^{\mathrm{T}}) \end{bmatrix} \\ &= \begin{bmatrix} \mathrm{Sk}(\boldsymbol{m}) & \boldsymbol{O} \\ \boldsymbol{O} & \mathcal{F}(\boldsymbol{m}) \end{bmatrix} \begin{bmatrix} \boldsymbol{B}(\boldsymbol{p}) \\ \nabla \boldsymbol{B}(\boldsymbol{p})^{\mathrm{T}} \end{bmatrix} \boldsymbol{I} \end{aligned} \tag{1.21}$$

where $\boldsymbol{O}$ represents the zero matrix, which is instrumental in analyzing the electromagnetic forces and torques in all three spatial dimensions. By knowing the magnetic moment of the object and the unit magnetic flux density in the three directions, the force and torque exerted on the object can be directly linked to the applied current.

The current applied is obtained from the voltage of the power supply. Its variation over time can be depicted as follows:

$$\frac{dI(t)}{dt} = \frac{V_c}{L_a} - \frac{R_a}{L_a} I(t) \tag{1.22}$$

where $I(t)$ denotes the current applied, while $\frac{dI(t)}{dt}$ signifies the rate at which the current changes. V_c, L_a, and R_a represent the voltage across the coil, the inductance, and the resistance of the coil, respectively. When multiple coils are activated concurrently, mutual induction may occur between adjacent coils, although it is typically negligible and often assumed to be zero in practical applications. Further analysis is provided in Section 1.2.3, with a visual representation in Figure 1.2b.

For particular applications, on-site calibration techniques have been established to simplify the process of determining magnetic field distributions. Analytical methods based on Maxwell's equations have been utilized to depict the magnetic scalar potential [34]. Polynomial regression, which incorporates the Laplace equation for flexible field mapping, has been applied in these calculations. The accuracy of these calculations was verified by comparing them with finite-element method simulation results, which can predict magnetic field distributions in new areas.

1.2.3 System Modeling and Control

In a simplified magnetic robot motion analysis, the quasistatic motion can be analyzed as [35]:

$$m\boldsymbol{v}(\dot{t}) = \boldsymbol{F}_m - \boldsymbol{c}\circ\boldsymbol{v}(t) + \Delta \tag{1.23}$$

where $\boldsymbol{v}(t)$ is the velocity of a controlled object, c is the total drag coefficient, $\circ$ denotes the element-wise product, and Δ represents the disturbance. Only $\boldsymbol{F}_m$ is controllable; the other variables vary with the surrounding environment and the controlled object.

In the electromagnetic system analysis, the dynamics of the magnetic field strength $\boldsymbol{H}(r)$ can be modeled based on the applied voltage $\boldsymbol{u}(t)$. As per Eq. (1.9), the magnetic field strength can be converted to magnetic flux density using the parameter magnetic permeability μ; thus, $\boldsymbol{H}(r)$ is utilized in the subsequent analysis.

To analyze the magnetic field strength $\boldsymbol{H}(r,t)$ in a circular region of radius a centered at the origin and surrounded by n electromagnets, as depicted in Figure 1.2b, the total magnetic field at position r and time t is given by $\boldsymbol{H}(r,t) = \sum_{k=1}^{n} \tilde{\boldsymbol{u}}_k(t)\boldsymbol{H}_k(r)$. Here, $\boldsymbol{H}_k(r) \in \mathbb{R}^3$ represents the magnetic field strength at position $r = [r_1, r_2, r_3]^T$ in 3D space, generated by the unit voltage from the center of the workspace.

In the analysis, only four electromagnets were taken into account, and a 2D space was utilized. $\boldsymbol{H}_0$ represents the magnetic field strength distribution around the lower right corner electromagnet and points to the right, while $\boldsymbol{H}_k(r)$ can be represented in global 2D coordinates using a rotation and translation matrix.

$$\boldsymbol{H}_k(\boldsymbol{r}) = -\boldsymbol{O}_k^T \boldsymbol{H}_0(a\boldsymbol{e} - \boldsymbol{O}_k \boldsymbol{r}) \tag{1.24}$$

where $\boldsymbol{e} = [1, 0]^T$ for 2D space analysis, and the rotation matrix $\boldsymbol{O}_k$ is represented as:

$$\boldsymbol{O}_k = \begin{bmatrix} \cos\left(\frac{2\pi(k-1)}{n}\right) & \sin\left(\frac{2\pi(k-1)}{n}\right) \\ -\sin\left(\frac{2\pi(k-1)}{n}\right) & \cos\left(\frac{2\pi(k-1)}{n}\right) \end{bmatrix} \tag{1.25}$$

The method described is a universal approach to depict the magnetic field distribution in a circular workspace surrounded by four electromagnets.

In high-gradient electromagnetic actuation systems, there is a presence of high resistance and inductance. The applied voltage is represented by the control input vector $\mathbf{u}(t) = [u_1(t), u_2(t), \dots, u_n(t)]^T$, and the voltage-state vector necessary for applying the magnetic field strength is denoted as $y_k(t) = R_k I_k(t)$.

The electromagnetic flux produced by the k^{th} electromagnet is given by $\phi_k = \sum_{j=1}^{n} L_{kj} I_j$. Consequently, $y_k = u_k - \dot{\phi}_k = u_k - L\dot{I}$. Thus, the state space equation can be formulated as follows:

$$\begin{cases} \boldsymbol{I}(t) = \boldsymbol{R}^{-1}\boldsymbol{\gamma}(t) \\ \dot{\boldsymbol{\gamma}}(t) = -\boldsymbol{R}\boldsymbol{L}^{-1}\boldsymbol{\gamma}(t) + \boldsymbol{R}\boldsymbol{L}^{-1}\boldsymbol{u}(t) \end{cases} \tag{1.26}$$

$$R = \mathrm{diag}(R_1, R_2, \dots, R_n); \quad I(t) = [I_1(t), I_2(t), \dots, I_n(t)]^T \tag{1.27}$$

where the inductance matrix $\boldsymbol{L} \in \mathbb{R}^{n\times n}$ is a symmetric constant matrix, the diagonal elements are L_{kk} denoted as the inductance of the k_{th} electromagnet, and $L_{jk} = L_{kj}$ is denoted as the mutual inductance between two electromagnets j and k. State space Eq. (1.26) can also be derived from Eq. (1.22).

The notation in Eq. (1.26) can be streamlined by defining $\xi\mathbf{A} = \mathbf{R}\mathbf{L}^{-1}$. If k electromagnets possess identical inductance and are symmetrically arranged, then all L_{kj} values are zero, allowing $\mathbf{A}$ to be the identity matrix. Consequently, the state space equation can be characterized by a single parameter ξ.

$$\boldsymbol{H}(r, t) = \boldsymbol{H}(r)\boldsymbol{\gamma}(t) \tag{1.28}$$

$$\boldsymbol{F}_m(r, t) = K\nabla\|\boldsymbol{H}(r, t)\|^2 \tag{1.29}$$

$$\boldsymbol{F}_m(r, t) = 2K\left\{\frac{\partial\,[\boldsymbol{H}(r)\boldsymbol{\gamma}(t)]}{\partial r}\right\}^T \boldsymbol{H}(r)\boldsymbol{\gamma}(t) = K_f g(\boldsymbol{r}(t), \boldsymbol{\gamma}(t)) \tag{1.30}$$

where K is volume and magnetic permeability-related parameters.

K_f contains the parameters ξ and K. The electromagnetic field is only related to the real-time position $r(t)$ and real-time voltage $\gamma(t)$, with a mapping of g().

According to Eqs. (1.23) and (1.30), the motion analysis is simplified to:

$$m\dot{\mathbf{v}}(t) = K_f g(\boldsymbol{r}(t), \gamma(t)) - \boldsymbol{c}\circ\mathbf{v}(t) + \Delta \tag{1.31}$$

According to Eqs. (1.26), (1.27), and (1.31), the complete dynamics of the electromagnetic actuator and the plant are:

$$\dot{\gamma}(t) = -\xi A\gamma(t) + \xi A\mathbf{u}(t) \tag{1.32}$$

$$\mathbf{v}(t) = \dot{\boldsymbol{r}}(t) \tag{1.33}$$

$$\dot{\mathbf{v}}(t) = \sigma_m K_f \mathbf{g}(\boldsymbol{r}(t), \gamma(t)) - \sigma_m \mathbf{c}\circ v(t) + \sigma_m \boldsymbol{\Delta} \tag{1.34}$$

where $\sigma_m = \frac{1}{m}$.

Preprogrammed control strategies are extensively employed across various applications, particularly in clinical settings where feedback is challenging to obtain [36, 37]. In such scenarios, the trajectory of the magnetic object is regulated by predefining the time-varying position sequence of the permanent magnet or the current input sequence to the electromagnetic system. For electromagnetic actuation systems, the effectiveness of the proposed method is significantly influenced by the coil design, and recent studies have highlighted the importance of optimizing coil design, which is emerging as a promising direction in MAS design.

Real-time acquisition of the magnetic moment is challenging. The necessary magnetic field is associated with the desired moment, as depicted in Eq. (1.14), which serves as a general solution for magnetic force control. This relationship is expressed by $\mathbf{m} = \mathcal{D}(\mathbf{B})$.

To symmetrically analyze and control the electromagnetic field and the gradient, according to Eqs. (1.19) and (1.21), the control input and output can be further represented as:

$$\begin{bmatrix} \mathbf{B} \\ \mathbf{F} \end{bmatrix} = \underbrace{\begin{bmatrix} \mathbb{I} & \mathbf{O} \\ \mathbf{O} & \mathcal{F}(\mathcal{D}(\mathbf{B})) \end{bmatrix}}_{\text{Second}} \underbrace{\begin{bmatrix} \mathbf{B}(\mathbf{p}) \\ \nabla\mathbf{B}(\mathbf{p})^{\mathrm{T}} \end{bmatrix}}_{\text{First}} \underbrace{\mathbf{I}}_{\text{Input}} \tag{1.35}$$

where $\mathbb{I} \subseteq \mathbb{R}^{3\times3}$, $\mathcal{D}(\mathrm{B})$ maps the magnetic field applied to the moment of controlled objects.

Equation (1.35) describes the physical process where the magnetic field and its gradient are produced using the current as an input. Subsequently, the controlled object acquires a magnetic moment through interaction with this magnetic field.

The preprogrammed control of MAS is categorized into three types based on the DOFs they control. The first category is 3-DOFs heading or rotational control. The second involves 3-DOFs force control, where the object’ moments are typically aligned with the applied magnetic field for superparamagnetism or constrained in a specific direction for magnetized ferromagnets. The third type encompasses 5-DOFs control, combining heading (2-DOFs) and force control (3-DOFs). In scenarios achieving full 6-DOFs control, the focus is on generating torque around the magnetized axis [38]. The challenge lies in controlling the magnetic torque, which is not aligned with the magnetization direction, under the assumption of nonuniformity.

The open-loop preprogrammed control method programs the necessary magnetic field—whether uniform, rotating, or oscillating—to achieve the desired motion or trajectory [39]. Additionally, this control strategy can manage swarm shape and shows potential in medical applications.

The field alignment force and torque control, as mentioned, are designed to direct the MMR toward the desired orientation. Disturbances caused by the attractive forces between MMRs and other factors can impact motion control. Consequently, the subsequent sections will concentrate on feedback-based control methods to improve the precision of preprogrammed control.

Figure 1.3a depicts the comprehensive control framework for the MAS, which includes three key components: the planning model, learning module, and control

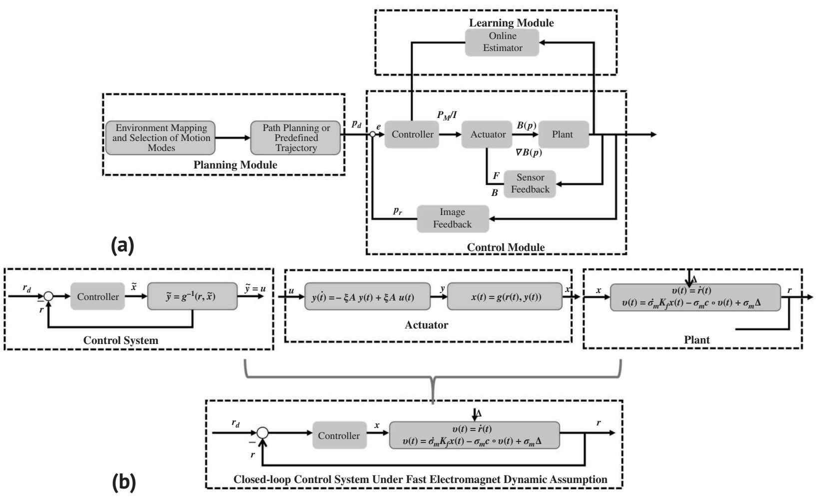

Figure 1.3 (a) General control scheme for MAS-based robot control with sensing feedback and online estimation. (b) The subsystems of the control system, actuation system, and plant; under the fast electromagnet dynamics assumption, the system can be simplified as the linear controller with the magnetic objects’ motion dynamics.

module. The planning module serves as the starting point, tasked with responsibilities such as environmental mapping and the selection of suitable locomotion strategies. It then proceeds to path planning. In certain scenarios where the trajectory is predetermined, a preset trajectory sequence is utilized in lieu of path planning [40, 41].

The control module assumes the role of devising a controller based on the established model. Most controllers are aimed at position or velocity control. To achieve a controlled position or velocity, the requisite position ($\boldsymbol{P_M}$) for the permanent magnet or the required current ($\boldsymbol{I}$) for the electromagnetic system is output to regulate the MAS. The real-time imaging feedback is usually harnessed to continually minimize the disparity between the real-time position ($\boldsymbol{p_r}$) and the desired position ($\boldsymbol{p_d}$). In certain applications, feedback mechanisms like Hall effect sensors or force sensors are crucial for refining the magnetic flux density (**B**) or force (**F**) by providing precise feedback [42]. The learning module is essential for estimating unknown parameters during dynamic modeling or controller design, enabling the system to learn and adapt to the magnetic actuation principle.

The complete dynamic system, comprising the actuator and the plant as described by Eqs. (1.32)–(1.34), can be analyzed by dissecting the nonlinear aspects. By distinguishing the linear and nonlinear components in Eq. (1.34), the nonlinear component can be characterized as:

$$\mathbf{x}(t) = \mathrm{g}(\boldsymbol{r}(t), \boldsymbol{\gamma}(t)) \tag{1.36}$$

where physical meaning of $\mathbf{x}(t)$ is the electromagnetic force.

Figure 1.3b presents the detailed equations for the block diagram of the controller, actuator, and plant. The applied voltage $u(t)$ serves as the input for the actuation system described by Eq. (1.32), while the state vector $\mathbf{x}(t)$ represents the electromagnetic force that connects the other two subsystems, as depicted by Eqs. (1.33) and (1.34).

Representing all vectors with state $\mathbf{x}$, the nonlinear system in Eq. (1.36) is represented as:

$$\mathbf{x} = \mathrm{g}(\boldsymbol{r}, \mathrm{g}^{-1}(\boldsymbol{r}, \boldsymbol{x})) \tag{1.37}$$

In practical applications, the dynamic system of electromagnetic actuation guarantees that the frequency of the subsystem described by Eq. (1.32) is much higher than that of the closed-loop control system dynamics. When A is an identity matrix, the system simplifies to the input $\boldsymbol{\gamma}(t)$ being asymptotically equivalent to the input $\boldsymbol{u}(t)$.

A nonlinear controller was proposed through feedback linearization with Eq. (1.38) as:

$$\hat{\boldsymbol{\gamma}} = \mathrm{g}^{-1}(\boldsymbol{r}, \tilde{\boldsymbol{x}}) \tag{1.38}$$

where $\tilde{\gamma}$ and $\tilde{\mathbf{x}}$ represent the estimated values of γ and $\mathbf{x}$, respectively. The controller design simplifies after cascading the nonlinear controller, as depicted by Eq. (1.38). Assuming rapid electromagnetic dynamics, the combined results are illustrated at the bottom of Figure 1.3b.

Many studies utilize a simplified system under the assumption of rapid electromagnetic dynamics to design controllers for position and velocity control. Classical controllers encompass linear types, such as proportional integral derivative control, linear-quadratic regulator control, and model predictive control [43, 44]. In certain applications, linear controllers and nonlinear filters are integrated into the system. Nonlinear controllers include adaptive and sliding mode control [45]. For autonomous control, the rapidly exploring random tree method is a common approach. In the learning model, iterative learning and deep learning are employed to estimate unknown parameters [46, 47], while a fuzzy logic-based control scheme is used for complex scenarios.

Preprogrammed control and dynamic magnetic field control are extensively used in clinical settings to accomplish tasks like selective embolization or stem cell delivery within high-viscosity joint fluid. Precise position control is crucial for accurate delivery applications, making feedback control particularly prevalent in intravenous drug delivery and endoscopy.

1.3 Development of Magnetic Actuation Systems

1.3.1 Development Phases and Trend of Magnetic Actuation Systems

In addition to systems with fixed electromagnets, reconfigurable systems have also been developed. These systems vary in their performance regarding magnetic actuation flexibility and precision: some excel in force control, while others show better torque control capabilities [48]. Some systems may encounter singularities, points where they lose the ability to generate specific forces or torques, or require excessive current near these points. To address these issues, adjustable MASs have been introduced. The BigMag system, for example, consists of six electromagnets placed in two fixtures. These fixtures can rotate around a common axis to avoid singularities and reduce total current, enabling the system to produce a strong magnetic field in any direction and at any point within the workspace (Figure 1.4a) [49, 50]. When all electromagnets are coplanar, the intersection angle between two adjacent ones is 60°. Chen et al. presented a system with four stationary and four movable electromagnets (Figure 1.4b) [51], similar to OctoMag but with independent adjustment of the upper set via robotic mechanisms. This design faces the challenge of balancing between a uniform magnetic field and a uniform field gradient.

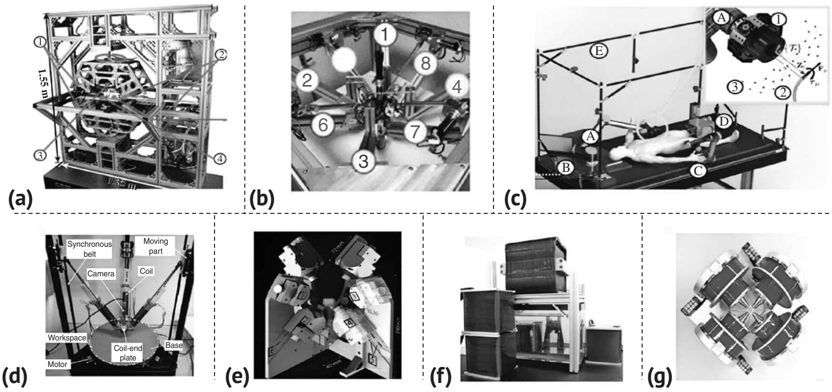

Figure 1.4 Magnetic actuation systems with movable electromagnets or novel designs: (a) BigMag system; (b) system with four stationary and four movable electromagnets; (c) ARMM system; (d) DeltaMag system; (e) BatMag system; (f) Omnimagnet system; (g) system comprising stepped cores. *Source*: Panel (a): Ref. [49] with permission of IEEE. Panel (b): Ref. [48] with permission of IEEE. Panel (c): Ref. [50] with permission of IEEE. Panel (d): Ref. [54] with permission of IEEE. Panel (e): Ref. [23] with permission of IEEE. Panel (f): Ref. [55] with permission of IEEE. Panel (g): Ref. [56] with permission of IEEE.

To address workspace constraints without enlarging electromagnet dimensions, driven mechanisms position mobile electromagnets closer to the region of interest (ROI). The Advanced Robotics for Magnetic Manipulation (ARMM) system pairs a cylindrical electromagnet with a 6-DOF UR10 robotic arm, generating precise magnetic fields at the ROI (Figure 1.4c) [52, 53]. Similarly, DeltaMag integrates three electromagnets into a parallel mechanism (Figure 1.4d), expanding workspace and reducing volume [54]. However, movable electromagnetic systems face challenges: electromagnets are bulkier and heavier than permanent magnets, and multi-coil setups with strong interaction forces are sometimes necessary. Integration with high-load, rigid, and compact drive mechanisms is crucial. Additionally, the total DOFs of drive mechanisms and coil currents can lead to multiple solutions and high nonlinearities, demanding robust, fast, and optimal field generation algorithms.

Several innovative designs have recently been introduced. Ongaro et al. developed the BatMag system, which uses nine electromagnets (Figure 1.4e) to independently control two devices in a 3D space by leveraging the inhomogeneity of strong magnetic fields [23]. Another design is a modular and reconfigurable MAS that uses multiple Omnimagents (Figure 1.4f) [55]. These can be temporarily rearranged during activation. Each Omnimagnet consists of a spherical core and three orthogonally arranged nested solenoids. The core's magnetization is determined by the currents in the three solenoids. Additionally, Li et al. developed a system with four electromagnets, each featuring a stepped core with a cone probe and a disk (Figure 1.4g) [56]. This optimized core shape enhances the magnetic field strength and gradient.

The use of MAS dates back to the 1920s [57], but researchers are still working to address the challenges that arise during its application by refining the system design. A permanent MAS creates a constant and uncontrollable magnetic field gradient. However, this feature restricts its application in certain scenarios where the magnets' positions are fixed due to the lack of controllability. To overcome this limitation, the orthogonal distributed electromagnetic system was developed. This system allows for controlled movement of magnetic objects in orthogonal directions and enables 3D position control through the use of six electromagnets. Despite these advantages, the system is limited by its working area, which makes clinical applications difficult.

The MAS design has evolved to incorporate nonorthogonal distributed electromagnets in response to the demand for greater controllability and enlarged working areas. This approach has gained mainstream status in MAS development. It addresses the limitations of the orthogonal design and enables more adaptable and accurate magnetic actuation for magnetic robots.

The permanent MAS, as detailed in Table 1.1, has some drawbacks, such as a constant and uncontrollable magnetic field gradient. However, it offers benefits like easily adjustable strength and lower costs, making it useful for certain applications. These applications include rotation control, localizing magnetic robots within defined workspaces [58], and particle sorting. Yet, its limitations, such as

Table 1.1 Advantages and disadvantages of different types of MASs.

Type	Advantages	Disadvantages
Permanent magnetic actuator	Easily adjustable magnitude; energy conservation and low cost; strong and stable magnetic field generation.	Limited DOFs; low frequency in a 3D environment; magnetic field cannot be immediately switched off.
Orthogonal distributed electromagnetic actuator	Controllable magnetic field; decoupled magnetic force in all dimensions.	Limited effective workspace; power consumption and heat dissipation.
Nonorthogonal distributed electromagnetic actuator	Larger effective workspace; higher magnetic field gradient.	Inflexible and bulky; power consumption and heat dissipation.
Robotic arm with a magnetic end effector	Extendable workspace; flexible, and easier to install.	Comparatively lower magnetic field gradient.

the unchangeable magnetic field gradient and limited control frequency, make it unsuitable for tasks that require precise positioning with quick on/off switching.

The orthogonal electromagnetic system allows for a manageable magnetic field gradient along orthogonal axes, enabling effective 3D position control with decoupling. However, its smaller operational range and increased heat production at high currents restrict its use in applications needing a bigger workspace or higher field gradient and torque.

The nonorthogonal electromagnetic system, unlike the orthogonal electromagnetic system, provides a bigger workspace, multidirectional controllability, and a higher field gradient or torque. This makes it suitable for surgical assistance, MMR delivery, and targeted drug delivery. However, these benefits are balanced by increased design and control complexity, higher energy consumption, and the risk of interference with other devices.

Recent studies have shown an increasing trend toward integrating the advantages of robotic arms and magnetic systems in MAS designs. This hybrid method can increase the system's workspace and flexibility, allowing for better control of MMRs in complex environments. One approach involves attaching a magnetic tip to a robotic arm to accurately position and manipulate MMRs [59]. Another method uses a robotic arm with multiple magnetic coils at its end to create a magnetic field gradient, helping to control microrobots or catheters with magnetic end effectors [60]. These hybrid systems greatly improve the precision and accuracy of magnetic robot control, making them ideal for clinical use. However, they are more complex than traditional MAS and may need advanced control algorithms and application conditions to optimize performance.

The classification of MAS types was based on papers documented from Google Scholar and the Web of Science databases between 2005 and 2024. After gathering the data, references in relevant publications were further screened. In the end, 42 high-quality papers and books were selected to illustrate the evolutionary trends of MAS types.

As depicted in Figure 1.5, systems with permanent magnet actuation were prevalent from 2005 to 2019. The combination of orthogonal and nonorthogonal electromagnetic systems, termed the electromagnetic actuation system, gained prominence from 2015 to 2024. Robotic arm-based systems saw significant development from 2020 to 2024. MAS research in clinical settings has evolved through several phases, with shifts in focus over time. Studies have progressed from system design to controller development, then to animal testing, and finally to human applications. Recent work on electromagnetic systems has centered on control theory and applications. For robotic arm-integrated systems, recent research has concentrated on system development, controller design, and application reporting within single studies.

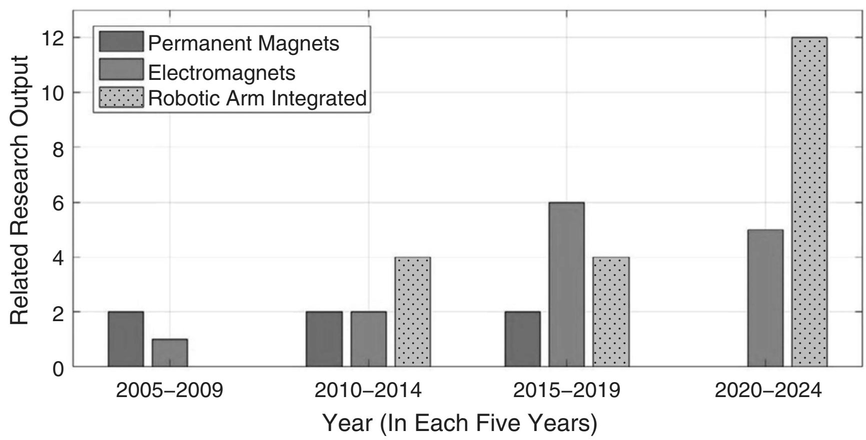

Figure 1.5 MAS development trend.

1.3.2 Development History of Electromagnetic Actuation Systems

The development timeline of electromagnetic actuation systems is illustrated on the right-hand side of Figure 1.6. Early designs were significantly influenced by the concepts of HC and MCs. Figure 1.6a presents a system that integrates HC and MCs to achieve 2D preprogrammed position control. However, clinical MAS applications require at least 3-DOFs control. The electromagnetic actuation system, equipped with multiple-DOF electromagnets, was designed to offer a large workspace and unconstrained DOFs (Figure 1.6b). The OctoMag was specifically developed to control intraocular microrobots for retinal surgery. An alternative method to increase the DOFs for magnetic robot manipulation involves using a dipole encircled by electrical wires, as depicted in Figure 1.6c.

Compared to traditional MAS designs, arranging multiple electromagnets around a workspace can generate a larger magnetic field gradient and workspace [61]. Figure 1.6d,e displays various nonorthogonal magnet arrangements. Adding an iron core greatly boosts the magnetic field strength and gradient from the electrical coils. In 2015, research indicated that a symmetrical system with a minimum of eight electromagnets could control all DOFs. This led to the development of an eight-electromagnet system with a back yoke. This enhanced catheter navigation system, with an enlarged workspace and magnetic field gradient, can perform ablation to treat cardiac arrhythmias. Experiments were done on a printed 3D model. Later, a similar design further expanded the workspace and enhanced the magnetic field gradient for use in multiple invasive therapies and diagnostics. After achieving system functionality and control, the focus shifted

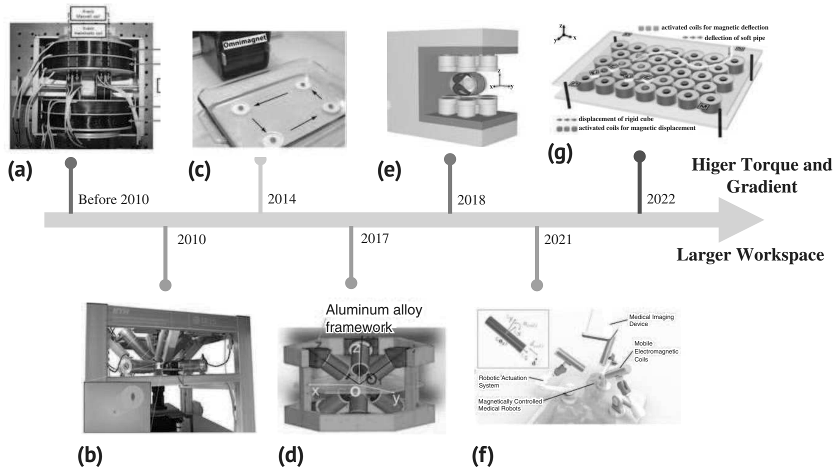

Figure 1.6 Development timeline for the electromagnetic actuators. (a) Two pairs of magnetic coil systems (HCs and MCs) to reach the locomotion in 2D. *Source*: Ref. [63] with permission of IOP Publishing. (b) OctoMag: 5-DOFs control under the electromagnetic field. *Source*: Ref. [64] with permission of IEEE. (c) Omnimagnet: a single stationary dipole source generates a fully controllable magnetic field and achieves 3D localization. *Source*: Ref. [65] with permission of IEEE. (d) Electromagnet-enhanced actuation system with a large workspace design for minimally invasive therapy. (e) Design of 18 copper coils distributed horizontally with a sufficiently large workspace for clinical applications. (f) Conceptual design of RoboMag in which three robotic arms are combined with three decoupled electromagnetic coils. (g) Planar electromagnetic array actuation system design applied in the deflection of soft pipes and displacement of rigid cubes.

to clinical-scale development. This system can be used for cardiac ablation in arrhythmia treatment or steering camera pills for GI diagnostic video acquisition. It has also been suggested for adaptive medical implants, like in adaptive radiation treatment for cancer therapy [62].

Table 1.2 presents a summary of the typical electromagnetic actuation systems intended for clinical use and their characteristics. The design standards took into account the controllable workspace, the maximum magnetic field intensity at the workspace’s center when the maximum current is applied, the highest attainable magnetic field gradient, and the dimensions of the objects being controlled. The count of electromagnets served as a benchmark to assess whether complete control over the system was achievable.

As indicated in Table 1.2, despite meeting all the listed requirements, there are still limitations in the design of orthogonal and nonorthogonal distributed electromagnetic actuation systems, such as rigidity and bulkiness. To tackle these issues, different arrangements of electromagnets, as illustrated in Figure 1.6f,g, have been

Table 1.2 Typical electromagnetic actuation systems and their properties.

	Workspace [mm]	**Center B_{max} [mT]**	**$\nabla B_{max}[Tm^1]$**	**Current [A]**	**Number of electromagnets**	**Size of the controlled object**
Octomag 2010	Hemisphere φ130	15	0.2	15	8	500 μm
Diller 2016	Cube 120 × 120 × 120	15	0.1	19	8	2 mm
Niu 2017	Sphere φ110	100	2.5	10	6	10 μm
Rahmer 2018	Cylindrical φ200	400	3	110–140	18	2 cm
Li 2019	Circle 2D φ50	139.2	20.5	10	4	100 μm
BatMag 2019	Sphere φ60 ≈ φ160	160	3.575	5	9	350 μm
ARMM 2019	Sphere φ1300	2350	45	20	1	Magnetically actuated catheters
RoboMag 2021	Hemisphere φ203	10	NA	5	3	500 nm microswarm
Array 2022	220.8 × 162.5 mm^2	20	1	Unit current	33	15 × 15 × 8 mm^3 cube and a soft magnetic pipe

proposed. Figure 1.4c presents the design of single or multiple robotic arms to achieve a more extensive workspace for applications in guiding surgical instruments within the human body. With this approach, the workspace can cover the entire human body, effectively addressing the problem of limited workspace.

Nonetheless, the magnetic flux intensity and gradient produced by a single electromagnet are constrained. When utilizing a single robotic arm along with an electromagnet, the magnetic gradient is fairly consistent within a radius of $r/2$ from the coil's center. Past this radius, the linearity of the gradient declines markedly. Hence, multiple electromagnets are integrated to intensify the magnetic field and gradient. As depicted in Figure 1.6f, it is recommended to place three electromagnets on top of three robotic arms positioned around the workspace. While the cooperative action of multiple electromagnets improves the working area and magnetic force, it also poses challenges for the analysis and control of the field distribution influenced by the movement of robotic arms. The application of a robotic arm-based system can be found in colonoscopy research [66], which was successfully executed in a pig. The time required for a single colonoscopy becomes shorter with autonomous magnetic manipulation. Level 3 autonomous inspection enhances the intelligence level in navigation within unstructured environments, bringing us one step closer to human application.

A different method, motivated by permanent magnet arrays, is to construct a 2D infinite space electromagnetic system, as shown in Figure 1.6g. Such a method addresses the constrained workspace issue in 3D space. Nevertheless, how to expand this kind of system into 3D space while preserving its features continues to be a difficult task.

1.4 Typical Applications of Magnetic Actuation Systems

The application of MAS in medical treatment dates back to 1985 with the use of an oscillating magnetic field for drug delivery. Significant advancements have been made in this field, particularly in applications targeting hard-to-reach areas within the human body that are promising for future use (see Figure 1.7).

This review focuses on developing novel medical treatments for various diseases. The benefits of MAS in surgery include improved precision, ease of use for novices, and reduced patient discomfort through minimally invasive and efficient procedures. Challenges in the operation of magnetic robots within the systems depicted in Figure 1.7 vary based on the disease characteristics and surgical environment.

Variety of environmental factors highlight the inherent differences in the system analysis of medical treatments across various regions of the human body.

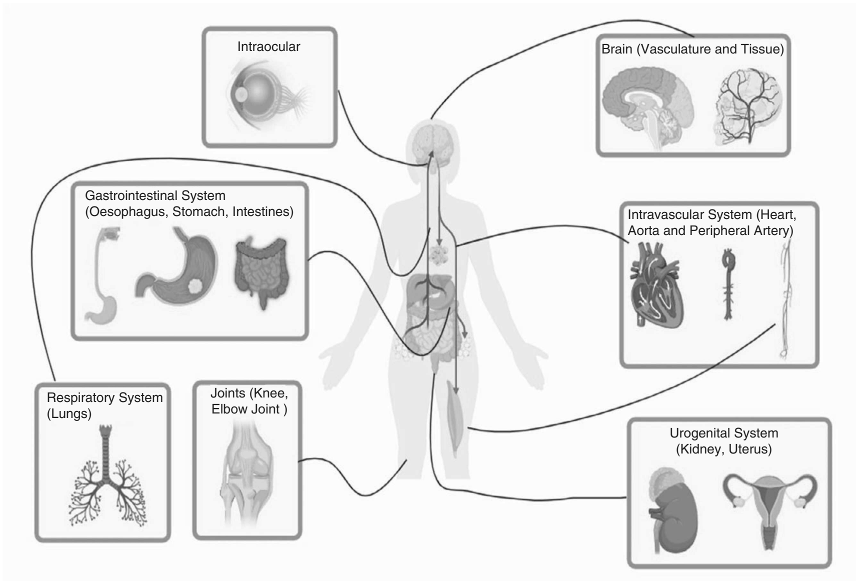

Figure 1.7 Potential environments for using MASs to control magnetic robots in hard-to-reach areas inside the human body.

For instance, intravascular applications require consideration of factors like blood flow speed and vessel size. The intra-ocular, GI, and respiratory systems, as well as human joints, offer natural pathways or accessible surfaces, making magnetic robots suitable for clinical access. Compared to naturally cavitated environments, the utility of MAS in medical treatment is evident in hard-to-reach areas where traditional robotic systems are inadequate. Notable examples include the brain, intravascular system, and urogenital system. Table 1.3 presents representative applications of seven different systems inside the human body, clinical application types, MASs employed, control methods, magnetic robots, imaging techniques, clinical stages, and tethering.

Beyond the typical examples, clinical applications in various human systems are clarified through experimental design, control algorithms, and validation. Control and actuation strategies differ according to the specific human systems or organs. To tackle the challenges of accessing these areas, studies have explored using untethered magnetized objects for drug or cell delivery, capsules with embedded magnets for endoscopy, and tethered continuum robots with magnetic end-effectors for surgery, supported by detailed clinical cases.

Table 1.3 Clinical applications of MASs.

Clinical applications	MASs	Control	Magnetic robot	Imaging	Clinical stage	Untethered
Brain tissue surgery	Permanent magnet array	Magnetic array trapping and motors	NdFeB with polymer housing	Fluoroscopic X-ray	Porcine brain	Y
Peripheral arterial disease surgery	Helmholtz coils	Magnetic sensor-based Preprogrammed control	Magnetic catheter	Digital microscope video	Vascular phantom	N
Aneurysm embolization	Robotic-assisted permanent MAS	Preprogrammed control	Self-adhesive microgels swarm	Fluoroscopy and US	Ex vivo human placenta	Y
Intravascular surgery	Helmholtz coils	Preprogrammed control	Claw-engaged microrobots	OCT catheter	Rabbit jugular vein	Y
Intraocular surgery	Electromagnetic actuation system	Preprogrammed control	Microrobot swarm	Camera/OCT	Bovine eye	Y
Knee cartilage regeneration	Electromagnetic actuation system	Precalibrated control	Medical microrobots	Optical microscope or arthroscope	Rabbit knee	Y
Gastrointestinal capsule endoscopy	Stereotaxis Niobe	Preprogrammed control	Video capsule	Fluoroscopy	Human	Y
Stomach ulcers treatment	Electromagnetic actuation system	Preprogrammed dynamic control	Soft film-like layers	Ultrasound imaging	Porcine stomach	Y
Lung inspection	8-coil MAS	Estimation-based catheter control	Magnetic endoscope	Camera	Lung phantom	N
Assisted urination	Permanent cubic magnet	Predefined field apply	Magnetic soft robotic bladder	Computed tomography	Porcine bladder	Y

1.4.1 Brain

The human brain is composed of the cerebrum, cerebellum, and brainstem, collectively termed brain tissue, with the remaining part being the brain's vascular surroundings. Research on MAS for animals (canine brains) dates back to 1990 [67] when a 5-mm-cylindrical permanent magnet was magnetically guided within the intraparenchymal brains of five adult canines to treat brain cancer, such as delivering drugs and taking biopsy samples. This study demonstrated the feasibility of remotely controlling untethered magnetized robots via a magnetic-driven system for clinical applications like placing hyperthermic heat lesions or targeted biopsies.

Recent studies have employed permanent magnet arrays to create a strong magnetic force trap, allowing robots to be drawn to traps without active control. A planar linear stage and one rotational axis were used to manipulate the microrobot's position within porcine brains. Ex vivo experiments on porcine brains, using fluorescent images for real-time tracking, highlighted the potential of MMRs in drug delivery, biopsies, hyperthermia, and cauterization, despite the study's limitation of a 6 cm workspace.

Controlling motion within the brain vasculature is another critical research area. Recent advanced research has developed cell-sized microrobots, equipped with real-time optoacoustic tracking for in vivo monitoring. The 3D real-time tracking of a microrobot within the murine cerebral vascular system has been accomplished for the first time. To simultaneously achieve imaging and magnetic response, the microrobot was coated with Ni and Au. Magnetic actuation was accomplished using a bar permanent magnet, with operations conducted manually. This successful experiment established a basis for safe and precise real-time procedures within the brain's vascular network.

1.4.2 Intravascular System

Deploying microrobots or catheters in human blood vessels faces a key challenge: navigating the varying vessel diameters to access the circulatory system. The human body has three main vessel types: arteries, veins, and capillaries, with diameters ranging from 25 mm in the aorta to 6 μm in capillaries. Large arteries, with diameters of 1–4 mm, are particularly important for intervention applications. Furthermore, their deeper location within muscle layers and thicker walls make arteries an ideal environment for interventions.

The successful use of endocardial catheters in medical interventions has been established for a decade [68], particularly in the milestone of human cardiac interventions using magnetic catheters for atrial fibrillation ablation. Myocardial ablation surgery, utilizing the commercial MAS named Stereotaxis Niobe to control the magnetic catheter tip under fluoroscopic imaging, is one of the few applications tested in humans. Other studies have documented related applications focusing on electrophysiological catheter guidance and control. Subsequent research has expanded to other heart diseases, including cardiac arrhythmias.

Current research initiatives are focused on developing solutions for a variety of diseases, such as peripheral arterial diseases and arterial aneurysms, by utilizing on-demand embolization techniques. In this context, microrobots have been developed to facilitate active retention during the process of drug delivery. Moreover, a continuum magnetic robot has been engineered with the aim of improving the access capability [69]. Simultaneously, the domain of soft robotics has been delving into the investigation of soft magnetic manipulation systems. The incorporation of soft magnetic actuation allows for greater flexibility in surgical procedures, which can be attributed to the implementation of remote magnetic control.

Peripheral arterial disease typically affects individuals aged 40 and older; it arises from narrowed blood vessels and may result in pain, impaired walking ability, and claudication. Percutaneous endovascular intervention stands as the principal treatment approach. The MAS plays a crucial role in steering the magnetic ring-tip catheter to the site of impairment and subsequently deploying a stent or balloon to unblock the vessel and restore its normal diameter. This method eliminates X-ray exposure through remote magnetic catheter control, with localization accomplished via catheter-tip sensing. A cylindrical configuration of Hall-effect sensors measures magnetic flux density in the workspace, permitting estimation of the magnetic catheter tip's location. Notwithstanding, X-ray imaging remains necessary for addressing bifurcations. The newly proposed magnetic-based localization algorithm enables real-time estimation of the magnetic tip's position. This approach has been practically applied using Helmholtz coils to manipulate the magnetic tip within the phantom.

Aneurysm is a condition where an artery's wall bulges outward. It can occur anywhere in the body, commonly in the aorta or brain. Due to their asymptomatic nature before rupture and the risk of severe internal bleeding, aneurysms have a high fatality rate. Embolization is an effective treatment strategy. Reference proposed a method of delivering microgels using magnetic-guided catheter assistance. This method combines C-arm fluoroscopy for real-time imaging with a magnetic robotic arm for catheter guidance. The self-adhesive microgel, delivered by the magnetic catheter and activated by an acidic stimulus to form connections, serves as an embolic agent. This study demonstrated the feasibility of controlling a swarm of microrobots in a dynamic human body environment to achieve effective embolization. The method was tested ex vivo on a human placenta. Ultrasound imaging confirmed effective aneurysm embolization, indicating that the microrobotic embolization platform is promising for application in human blood vessels.

Most intravascular applications rely on tethered magnetic catheters due to blood flow velocity. Steering untethered microrobots in the bloodstream poses a key challenge because of the circulatory system's rapid blood flow. To address this, a novel solution was proposed with an active retention structure. The microrobot features a claw to stay in place within blood vessels. This unique mechanism allows microrobots to remain positioned in the blood environment despite strong blood flow. This structure's successful use in a live rabbit's jugular vein has enabled the application of untethered microrobot swarms for treating vascular diseases and circulatory drug delivery via noninvasive methods.

To enhance the capability of a tethered catheter, researchers designed a novel untethered helical magnetic robot for better endovascular access. This robot features an articulating magnetic tip to improve steerability and a helical protrusion for rotation and forward motion energy generation. The system includes a central working channel for fluid injection. X-ray radiography monitors the robot's position in the vascular system in real-time. A commercial electromagnetic system called Navion controls the magnetic robot, achieving broad directional catheter control. An ex vivo experiment confirmed the helical structure's effectiveness in driving the robot forward. Further experiments using human placental blood vessels ex vivo and a porcine model in vivo validated the robot and system's effectiveness. Comparisons between the commercial and new catheters in the live pig study showed the new design's advantage in moving backward without vessel damage.

1.4.3 Intraocular System

In intraocular procedures, maintaining the stability of the surgeon's hand is crucial. As a result, significant research efforts have been dedicated to creating mechanical systems that can ensure a steady hand during surgical operations. Experiments conducted on chicken embryos and phantom models that mimic the human eye have contributed to this goal. Additionally, the development of robotic arms designed to reduce surgeons' hand tremors has been actively pursued.

Recent advancements in magnetically driven systems have sparked interest in exploring minimally invasive solutions for intraocular applications. In a 2010 study, localization was accomplished using a single camera, which demonstrated effectiveness in a model eye and laid the groundwork for future surgical procedures. Later, an in vivo rabbit eye experiment further confirmed the potential in this field [70]. Researchers developed a cylindrical microrobot, sized at 285 μm in diameter and 1.8 mm in length, to fit into a needle for easy injection into the eye. The Octomag system allows for intraocular surgery beneath the MAS, reserving space for imaging and surgical procedures upfront. Intraocular surgery offers imaging benefits due to its surface exposure. However, human trials are pending due to uncontrollably rapid motions during drug delivery. In material removal surgeries on the ocular globe, precise force control is essential, keeping its application in the animal trial phase. Recent research has explored targeted therapy via rotating-gradient magnetic fields. The success of this method in bovine eyes shows that magnetized microbots, driven by preprogrammed fields, can effectively deliver drugs in intraocular settings.

1.4.4 Knee and Elbow Joints

Knee and elbow joint cartilage damage is commonplace in athletes and the elderly, with a rising incidence among young adults in recent times. The standard approach to tackle this issue relies on arthroscopy for imaging. Regrettably, conventional therapeutic approaches do not provide means for fully restoring the damaged cartilage. Current treatments mainly focus on reducing inflammation and draining joint fluid to promote self-healing. The most cutting-edge method is platelet-rich plasma (PRP) injection, which delivers concentrated platelets to the injury site to alleviate pain and accelerate repair. However, the outcomes of this method are not uniformly remarkable, and its effectiveness varies significantly among individuals.

An alternative solution frequently suggested for treating serious cartilage injury is the utilization of stem cells. Mesenchymal stem cells (MSCs) can be easily obtained from placental tissue or umbilical cord blood. This novel method involves loading MSCs onto porous microrobots. These robots are injected into the affected joint via a needle and controlled by the MAS. Magnetic navigation enables precision medicine. As a 2020 study recorded [15], human adipose-derived MSCs can aid knee cartilage regeneration. Experiments employed a rabbit knee cartilage defect model. As the medical field increasingly accepts stem cell theory for therapy, this approach shows great potential for curing intra-articular damage clinically.

1.4.5 GI System

The GI system contains natural channels with relatively large spaces, making it easier for devices like millirobots, capsules, or catheters to navigate. Endoscopy is vital for GI malfunction diagnosis. Colonoscopy, gastroscopy, and esophagoscopy are used to examine the intestines, stomach, and esophagus respectively.

Early work on video capsules driven by Stereotaxis Niobe showed that navigating a 3D environment is central to GI endoscopy. Because the gut is much larger than intraocular spaces, the system must provide an extensive workspace while maintaining precise positioning. Researchers therefore combined robotic-arm actuators with refined control schemes: a rotary stage ending in a permanent magnet steered the capsule endoscope. The next year, further evaluation in a fluid-filled, mock-up stomach confirmed high robustness under reduced control frequency, localization errors, field misalignment, and singular configurations.

These two investigations established both the hardware layout and the algorithms required for complex tasks. As capsule endoscopy in the GI tract matured, later studies shifted toward smarter magnetic actuation, autonomy, and collaborative operation [71]. Reference examined colonoscopy with a focus on autonomy and intelligence. Higher autonomy not only lowers cost but also improves patient comfort, thereby promising broad clinical uptake of GI endoscopy.

Over the past few years, there has been a proposal to employ microrobots in stomach incision treatment, representing a nascent field of study that is still at the cellular slice stage. The design draws inspiration from the frictional anisotropy of micro-walkers, which mimics the process of walking. The most recent research has also highlighted this design approach, referred to as the asymmetrical friction effect, induced by magnetic torque. Enhancing the design of magnetic robots can considerably bolster the magnetic actuation methods applied in clinical settings. The rise of applications for precise drug delivery and surgical assistance in the stomach indicates that magnetic actuation technology, along with its control algorithms, has reached a certain level of maturity.

Recent research has explored using multiple microrobots to perform tasks. By dynamically controlling the magnetic field, researchers can manipulate a multilayer, film-like soft robot. The layers can separate under a predefined magnetic field and fix at different spots to treat stomach ulcers. These experiments were performed on a porcine stomach to address multiple ulcers.

1.4.6 Respiratory System

The respiratory system comprises the respiratory tract and lungs. The respiratory tract is divided into the upper portion (which includes the nose, mouth, pharynx, and throat) and the lower portion (which consists of the windpipe, bronchial tubes, and lungs). While the components of the upper respiratory tract are relatively easy to access, the lower respiratory tract, particularly the bronchial tubes and lungs, presents a complex situation. The subsequent discussion will primarily focus on the intricate areas of the respiratory system.

A position estimation method based on lung phantom experiments has been proposed [72]. When controlling an endoscope in the lung, positioning is the key difficulty. The approach uses images detected by the endoscope to determine the catheter's current position. The device's kinematics are captured by comparing input with visual feedback. This novel approach allows for real-time positioning within the human lung structure.

Bronchoscopy is vital for detecting diseases in the bronchial tubes. Optimizing the navigation trajectory is essential for smooth and autonomous detection. This has led to the development of a soft magnetic catheter, activated by two robot-driven permanent magnets. The goal is to enhance the navigation path for autonomous and atraumatic detection within the bronchial tubes, as highlighted by Pittiglio. By deploying a specially designed soft catheter robot, autonomous disease detection within the bronchial tree phantom has been achieved, with significant implications for medical diagnostics and interventions. This atraumatic autonomous endoscopy is possible through two robotic arms collaborating to control a patient-specific magnetic catheter. The robotic arms are programmed to follow a predefined trajectory, minimizing contact during navigation. A comparative study of four catheters using a leader-follower algorithm showed greatly improved tracking accuracy and reduced targeting errors.

1.4.7 Urogenital System

The urogenital system is composed of two parts: the urinary and genital tracts. The urinary tract includes key components such as the kidney, ureter, bladder, and urethra. One common ailment in the urogenital system is kidney stones. Retrograde intrarenal surgery is a procedure used to remove these stones. The endoscope passes through the urine storage area, enters the kidney, locates the stone, and then breaks it up using a laser.

Flexible magnetic continuum robots have been developed for use in the urogenital system. A catheter with a magnetic tip is used to navigate through a kidney phantom. The control method can predict the nonlinear behavior of the continuum robot in a heterogeneous magnetic field. In 2022, a novel application demonstrated that a specially designed magnetic soft robotic bladder could enhance contraction through magnetic actuation [73]. This innovation has potential for assisted urination. Its safety was tested in a porcine model over two weeks. The genital tract is divided into the female and male reproductive systems. In the male reproductive system, physical contraception is a key application. Research has led to the development of wireless robots for this purpose. Their potential has been shown through applications in a tubular phantom with ultrasound guidance.

1.5 Scope and Layout of the Book

The primary scope of this book is to bridge the existing gap in current literature, where the focus has predominantly been on the fabrication and individual design of small-scale robots, often overlooking the systematic design methodology of the external actuation systems required to manipulate them. Consequently, this text is dedicated to the comprehensive study of mobile MASs, summarizing the latest advancements in their design, control strategies, experimental validation, and performance optimization. Unlike stationary systems, the mobile MASs discussed herein are characterized by their ability to provide large workspaces, rapidly varied magnetic fields, and versatile system configurations with high scalability and bandwidth. The content is structured to guide readers—ranging from postgraduate students to researchers in robotics, control, and biomedical engineering—through the transition from manual and semi-automated operations toward fully adaptive, intelligent manipulation suited for complex tasks such as active targeted delivery and remote sensing.

The layout of the book is organized into 10 chapters that progress logically from fundamental principles to advanced system designs and specific applications. The text begins in Chapter 1 by establishing the necessary background, introducing the basic concepts, actuation principles, and the historical development of magnetic actuation technology. Following this foundational introduction, the book immediately addresses modern design challenges in Chapter 2, which focuses on the design and real-time optimization of actuation systems with enhanced flexibility, demonstrating capabilities such as autonomous navigation under ultrasound Doppler imaging. To tackle the complexities of controlling soft miniature robots, Chapter 3 introduces a deep reinforcement learning framework, highlighting the intersection of modern artificial intelligence with magnetic manipulation control.

The middle chapters of the book provide an in-depth technical analysis of specific system configurations and control methodologies. Chapters 4 and 5 explore reconfigurable electromagnetic actuation systems designed for large workspaces, detailing multi-objective optimization methods for coil configuration generation as well as performance-guided strategies for field and force control. This is followed by a comprehensive examination of parallel-mobile-coil systems in Chapters 6 and 7, which cover multimode control, mechanism design, and parameter optimization. These chapters also present advanced applications of these systems, such as motion planning for autonomous microrobotic navigation in dynamic flowing conditions, thereby validating the theoretical models through rigorous simulation and experimentation.

The final section of the book emphasizes practical implementation in medical and engineering contexts. Chapter 8 presents a magnetically controlled guidewire robotic system specifically designed for vascular intervention, including mathematical modeling and in vivo validation of multistage embolization strategies. Chapter 9 extends the discussion to wired magnetic microrobots utilizing parallel-mobile-coil systems. The book concludes in Chapter 10 with a summary of design methodologies and integration strategies between imaging and actuation systems. It offers a forward-looking perspective on the future of the field, predicting that mobile MASs will become increasingly intelligent and self-adaptive over the next five years, further expanding their utility in translational biomedicine and interdisciplinary research.

References

1 S. Palagi and P. Fischer. Bioinspired microrobots. *Nature Reviews Materials*, 3(6): 113–124, 2018.

2 M. Sitti. Miniature soft robots—road to the clinic. *Nature Reviews Materials*, 3(6): 74–75, 2018.

3 G.-Z. Yang, et al. The grand challenges of science robotics. *Science Robotics*, 3(14): eaar7650, 2018.

4 S. Jeon, et al. Magnetically actuated microrobots as a platform for stem cell transplantation. *Science Robotics*, 4: eaav4317, 2019.

5 S. Lee, S. Lee, S. Kim, C. Yoon, H. Park, J. Kim, and H. Choi. Fabrication and characterization of a magnetic drilling actuator for navigation in a three-dimensional phantom vascular network. *Scientific Reports*, 8(1): 3691, 2018.

6 Y. Kim, G. A. Parada, S. Liu, and X. Zhao. Ferromagnetic soft continuum robots. *Science Robotics*, 4(33): eaax7329, 2019.

7 D. Son, H. Gilbert, and M. Sitti. Magnetically actuated soft capsule endoscope for fine-needle biopsy. *Soft Robotics*, 7(1): 10–21, 2020.

8 M. Xie, A. Shakoor, Y. Shen, J. K. Mills, and D. Sun. Out-of-plane rotation control of biological cells with a robot-tweezers manipulation system for orientation-based cell surgery. *IEEE Transactions on Biomedical Engineering*, 66(1): 199–207, 2018.

9 Y. Deng, A. Paskert, Z. Zhang, R. Wittkowski, and D. Ahmed. An acoustically controlled helical microrobot. *Science Advances*, 9(38): eadh5260, 2023.

10 A. Aghakhani, O. Yasa, P. Wrede, and M. Sitti. Acoustically powered surface-slipping mobile microrobots. *Proceedings of the National Academy of Sciences*, 117(7): 3469–3477, 2020.

11 G. Kosa and P. Hunziker. Small-scale robots in fluidic media. *Advanced Intelligent Systems*, 1(7): 1900035, 2019.

12 L. Daneshmandi, et al. Emergence of the stem cell secretome in regenerative engineering. *Trends in Biotechnology*, 38(12): 1373–1384,2020.

13 J. Li, et al. Reconfigurable magnetic microrobot swarm: multimode transformation, reconfigurable swarm, and intensive killing of cancer cells. *Science Robotics*, 3(19): eaat8829, 2018.

14 T. Wei, et al. Development of magnet-driven and image-guided degradable microrobots for the precise delivery of engineered stem cells for cancer therapy. *Small*, 16(41): 1906908, 2020.

15 G. Go, et al. Human adipose–derived mesenchymal stem cell–based medical microrobot system for knee cartilage regeneration in vivo. *Science Robotics*, 5(38): eaay6626, 2020.

16 L. Zheng, Y. Jia, D. Dong, W. Lam, D. Li, H. Ji, and D. Sun. 3D navigation control of untethered magnetic microrobot in centimeter-scale workspace based on field-of-view tracking scheme. *IEEE Transactions on Robotics*, 38(3): 1583–1598, 2021.

17 D. Dong, L. Xing, L. Zheng, Y. Jia, and D. Sun. Automated 3-D electromagnetic manipulation of microrobot with a path planner and a cascaded controller. *IEEE Transactions on Control Systems Technology*, 30(6): 2672–2680, 2021.

18 Q. Boehler, S. Gervasoni, S. L. Charreyron, C. Chautems, and B. J. Nelson. On the workspace of electromagnetic navigation systems. *IEEE Transactions on Robotics*, 39(1): 791–807, 2022.

19 L. Yang, Z. Yang, M. Zhang, J. Jiang, H. Yang, and L. Zhang. Optimal parameter design and microrobotic navigation control of parallel-mobile-coil systems. *IEEE Transactions on Automation Science and Engineering*, 21(1): 855–867, 2022.

20 H. Xie, et al. Reconfigurable magnetic microrobot swarm: multimode transformation, locomotion, and manipulation. *Science Robotics*, 4: eaav8006, 2019.

21 D. Ahmed, A. Sukhov, D. Hauri, D. Rodrigue, G. Maranta, J. Harting, and B. J. Nelson. Bioinspired acousto-magnetic microswarm robots with upstream motility. *Nature Machine Intelligence*, 3: 311–320, 2021.

22 X. Yang, R. Tan, H. Lu, T. Fukuda, and Y. Shen. Milli-scale cellular robots that can reconfigure morphologies and behaviors simultaneously. *Nature Communications*, 13(1): 4156, 2022.

23 F. Ongaro, S. Pane, S. Scheggi, and S. Misra. Design of an electromagnetic setup for independent three-dimensional control of pairs of identical and nonidentical microrobots. *IEEE Transactions on Robotics*, 35(1): 174–183, 2019.

24 Z. Li, et al. Human mesenchymal stem cell-derived miniature joint system for disease modeling and drug testing. *Advanced Science*, 9(21): 2105909, 2022.

25 P. Wrede, et al. Real-time 3D optoacoustic tracking of cell-sized magnetic microrobots circulating in the mouse brain vasculature. *Science Advances*, 8(19): eabm9132, 2022.

26 Q. Wang and L. Zhang. External power-driven microrobotic swarm: from fundamental understanding to imaging-guided delivery. *ACS Nano*, 15(1): 149–174, 2021.

27 J. Yu, L. Yang, and L. Zhang. Pattern generation and motion control of a vortex-like paramagnetic nanoparticle swarm. *The International Journal of Robotics Research*, 37(8): 912–930, 2018.

28 L. Yang, J. Jiang, X. Gao, Q. Wang, Q. Dou, and L. Zhang. Autonomous environment-adaptive microrobot swarm navigation enabled by deep learning-based real-time distribution planning. *Nature Machine Intelligence*, 4(5): 480–493, 2022.

29 A. J. Petruska and B. J. Nelson. Minimum bounds on the number of electromagnets required for remote magnetic manipulation. *IEEE Transactions on Robotics*, 31(3): 714–722, 2015.

30 C. R. Thornley, L. N. Pham, and J. J. Abbott. Reconsidering six-degree-of-freedom magnetic actuation across scales. *IEEE Robotics and Automation Letters*, 4(3): 2325–2332, 2019.

31 M. Parker. Magnetic traps help robots navigate soft tissue. *Nature Electronics*, 4: 770, 2021.

32 B. Shapiro, S. Kulkarni, A. Nacev, S. Muro, P. Y. Stepanov, and I. N. Weinberg. Wiley interdiscip. *Wiley Interdisciplinary Reviews: Nanomedicine and Nanobiotechnology*, 7: 446, 2015.

33 L. Xing, D. Li, H. Cao, L. Fan, L. Zheng, L. Zhang, and D. Sun. High-efficiency automatic catheter navigation system with a 3D magnetic-field-drive mechanism. *Advanced Intelligent Systems*, 4: 2100214, 2022.

34 Y. Xing, Y. Jia, Z. Zhan, J. Li, and C. Hu. Modeling and control of a soft magnetic micro-swimmer. In *2021 International Conference on Robotics and Automation (ICRA)*, pages 7281–7287, Piscataway, NJ, 2021. IEEE.

35 D. Son, M. C. Ugurlu, and M. Sitti. Permanent magnet array–driven navigation of wireless millirobots inside soft tissues. *Science Advances*, 7(43): eabi8932, 2021.

36 D. Jin, et al. Swarming self-adhesive microgels enabled aneurysm on-demand embolization in physiological blood flow. *Science Advances*, 9(19): eadf9278, 2023.

37 T. Li, et al. Bioinspired claw-engaged and biolubricated swimming microrobots creating active retention in blood vessels. *Science Advances*, 9(18): eadg4501, 2023.

38 A. J. Petruska. Open-loop orientation control using dynamic magnetic fields. *IEEE Robotics and Automation Letters*, 5(4): 5472–5476,2020.

39 T. Xu, C. Huang, Z. Lai, and X. Wu. Independent control strategy of multiple magnetic flexible millirobots for position control and path following. *IEEE Transactions on Robotics*, 38: 2875, 2022.

40 Q. Zou, X. Du, Y. Liu, H. Chen, Y. Wang, and J. Yu. Dynamic path planning and motion control of microrobotic swarms for mobile target tracking. *IEEE Transactions on Automation Science and Engineering*, 20: 2454–2468, 2022.

41 M. Salehizadeh and E. D. Diller. Path planning and tracking for an underactuated two-microrobot system. *IEEE Robotics and Automation Letters*, 6: 2674, 2021.

42 J. Wu, K. Yu, I. Lopez, A. A. Izquierdo, H. Saber, F. Alambeigi, and L. Zhou. Integrated magnetic location sensing and actuation of steerable robotic catheters for peripheral arterial disease treatment. *IEEE Robotics and Automation Letters*, 8: 5656, 2023.

43 J. Liu, T. Xu, and X. Wu. Optimal planning of internet data centers decarbonized by hydrogen-water-based energy systems. *IEEE Transactions on Automation Science and Engineering*, 20: 1577, 2023.

44 J. Jiang, L. Yang, and L. Zhang. Closed-loop control of a Helmholtz coil system for accurate actuation of magnetic microrobot swarms. *IEEE Robotics and Automation Letters*, 6: 827, 2021.

45 S. O. Demir, U. Culha, A. C. Karacakal, A. Pena-Francesch, S. Trimpe, and M. Sitti. Task space adaptation via the learning of gait controllers of magnetic soft millirobots. *The International Journal of Robotics Research*, 40: 1331, 2021.

46 J. Liu, X. Wu, C. Huang, L. Manamanchaiyaporn, W. Shang, X. Yan, and T. Xu. 3-D autonomous manipulation system of helical microswimmers with online compensation update. *IEEE Transactions on Automation Science and Engineering*, 18: 1380, 2020.

47 T. Xu, J. Liu, C. Huang, T. Sun, and X. Wu. Discrete-time optimal control of miniature helical swimmers in horizontal plane. *IEEE Transactions on Automation Science and Engineering*, 19: 2267, 2021.

48 R. Chen, D. Folio, and A. Ferreira. Performance metrics for a robotic actuation system using static and mobile electromagnets. In *2019 International Conference on Robotics and Automation (ICRA)*, page 2474, Montreal, 2019. IEEE.

49 J. Sikorski, I. Dawson, A. Denasi, E. E. Hekman, and S. Misra. Introducing BigMag – a novel system for 3D magnetic actuation of flexible surgical manipulators. In *2017 IEEE International Conference on Robotics and Automation (ICRA)*, page 3594, Singapore, 2017. IEEE.

50 J. Sikorski, A. Denasi, G. Bucchi, S. Scheggi, and S. Misra. Vision-based 3-D control of magnetically actuated catheter using BigMag—an array of mobile electromagnetic coils. *IEEE/ASME Transactions on Mechatronics*, 24: 505, 2019.

51 R. Chen, D. Folio, and A. Ferreira. Study of robotized electromagnetic actuation system for magnetic microrobots devoted to minimally invasive ophthalmic surgery. In *2019 IEEE International Symposium on Medical Robotics (ISMR)*, page 1, Atlanta, GA, 2019. IEEE.

52 J. Sikorski, C. M. Heunis, F. Franco, and S. Misra. The ARMM system: an optimized mobile electromagnetic coil for non-linear actuation of flexible surgical instruments. *IEEE Transactions on Magnetics*, 55: 1, 2019.

53 C. M. Heunis, Y. P. Wotte, J. Sikorski, G. P. Furtado, and S. Misra. The ARMM system-autonomous steering of magnetically-actuated catheters: towards endovascular applications. *IEEE Robotics and Automation Letters*, 5: 704, 2020.

54 L. Yang, X. Du, E. Yu, D. Jin, and L. Zhang. DeltaMag: an electromagnetic manipulation system with parallel mobile coils. In *2019 International Conference on Robotics and Automation (ICRA)*, page 9814, Montreal, 2019. IEEE.

55 A. J. Petruska, J. B. Brink, and J. J. Abbott. First demonstration of a modular and reconfigurable magnetic-manipulation system. In *2015 IEEE International Conference on Robotics and Automation (ICRA)*, page 149, Seattle, WA, 2015. IEEE.

56 D. Li, F. Niu, J. Li, X. Li, and S. Dong. Gradient-enhanced electromagnetic actuation system with a new core shape design for microrobot manipulation. *IEEE Transactions on Industrial Electronics*, 67: 4700, 2020.

57 A. Heilbronn. Eine neue methode zur bestimmung der viskosität lebender protoplasten. *Jahrbücher für Wissenschaftliche Botanik*, 61: 284, 1922.

58 C. Watson and T. K. Morimoto. Permanent magnet-based localization for growing robots in medical applications. *IEEE Robotics and Automation Letters*, 5: 2666, 2020.

59 J. S. Barajas-Gamboa, et al. First in-human experience with a novel robotic platform and magnetic surgery system. *International Journal of Medical Robotics and Computer Assisted Surgery*, 17: 1, 2021.

60 X. Du, et al. Real-time navigation of an untethered miniature robot using mobile ultrasound imaging and magnetic actuation systems. *IEEE Robotics and Automation Letters*, 7: 7668, 2022.

61 J. Rahmer, C. Stenging, and B. Gleich. Remote magnetic actuation using a clinical scale system. *PLoS One*, 13: e0193546, 2018.

62 J. Rahmer, C. Stehning, and B. Gleich. Spatially selective remote magnetic actuation of identical helical micromachines. *Science Robotics*, 2: eaal2845, 2017.

63 H. Choi, J. Choi, G. Jang, J. Park, and S. Park. Two-dimensional actuation of a microrobot with a stationary two-pair coil system. *Smart Materials and Structures*, 18(5): 055007, 2009.

64 M. P. Kummer, J. J. Abbott, B. E. Kratochvil, R. Borer, A. Sengul, and B. J. Nelson. OctoMag: an electromagnetic system for 5-DOF wireless micromanipulation. *IEEE Transactions on Robotics*, 26(6): 1006–1017, (2010).(b) *IEEE Transactions on Robotics*(c) *IEEE Transactions on Robotics*(d)

65 A. J. Petruska, A. W. Mahoney, and J. J. Abbott. Remote manipulation with a stationary computer-controlled magnetic dipole source. *IEEE Transactions on Robotics*, 30(5): 1222–1227, 2014.(b) *IEEE Transactions on Robotics*(c)

66 J. W. Martin, B. Scaglioni, J. C. Norton, V. Subramanian, A. Arezzo, K. L. Obstein, and P. Valdastri. Enabling the future of colonoscopy with intelligent and autonomous magnetic manipulation. *Nature Machine Intelligence*, 2(10): 595–606, 2020.

67 M. S. Grady, M. A. III Howard, J. A. Molloy, R. C. Ritter, E. G. Quate, and G. T. Gillies. Nonlinear magnetic stereotaxis: three-dimensional, *in vivo* remote magnetic manipulation of a small object in canine brain. *Medical Physics*, 17: 405, 1990.

68 F. Carpi and C. Pappone. Stereotaxis Niobe® magnetic navigation system for endocardial catheter ablation and gastrointestinal capsule endoscopy. *Expert Review of Medical Devices*, 6: 487, 2009.

69 M. Richter, M. Kaya, J. Sikorski, L. Abelmann, V. Kalpathy Venkiteswaran, and S. Misra. Magnetic soft helical manipulators with local dipole interactions for flexibility and forces. *Soft Robotics*, 10: 647–659,2023.

70 F. Ullrich, et al. Mobility experiments with microrobots for minimally invasive intraocular surgery. *Investigative Ophthalmology & Visual Science*, 54: 2853, 2013.

71 S. Kim, S. Bae, W. Lee, and G. Jang. Magnetic navigation system composed of dual permanent magnets for accurate position and posture control of a capsule endoscope. *IEEE Transactions on Industrial Electronics*, 71: 739, 2024.

72 J. Edelmann, A. J. Petruska, and B. J. Nelson. Estimation-based control of a magnetic endoscope without device localization. *Journal of Medical Robotics Research*, 3: 1850002, 2018.

73 Y. Yang, et al. Magnetic soft robotic bladder for assisted urination. *Science Advances*, 8(34): eabq1456, 2022.